Cellular cryo-tomography of nidovirus replication organelles

Wolff, G.

CHAPTER 4

A molecular pore spans the double membrane of the coronavirus replication organelle

Georg Wolff [1], Ronald W.A.L. Limpens [1], Jessika C. Zevenhoven-Dobbe [2], Ulrike Laugks [3], Shawn Zheng [4], Anja W.M. de Jong [1], Roman I. Koning [1], David A. Agard [5], Kay Grünewald [3,6], Abraham J. Koster [1], Eric J. Snijder [2], Montserrat Bárcena [1]

[1] Section Electron Microscopy, Department of Cell and Chemical Biology, Leiden University Medical Center, Leiden, The Netherlands.

[2] Molecular Virology Laboratory, Department of Medical Microbiology, Leiden University Medical Center, Leiden, The Netherlands.

[3] Department of Structural Cell Biology of Viruses, Centre for Structural Systems Biology, Heinrich Pette Institute, Leibnitz Institute of Experimental Virology, 22607 Hamburg, Germany.

[4] Howard Hughes Medical Institute, Department of Biochemistry and Biophysics, University of California San Francisco, San Francisco, CA 94143, USA.

[5] Department of Biochemistry and Biophysics, University of California San Francisco, San Francisco, CA 94143, USA.

[6] Department of Chemistry, MIN Faculty, Universität Hamburg, 20146 Hamburg, Germany.

Published in Science: doi.org/10.1126/science.abd3629

Abstract

Coronavirus genome replication is associated with virus-induced cytosolic double-membrane vesicles, which may provide a tailored microenvironment for viral RNA synthesis in the infected cell. However, it is unclear how newly synthesized genomes and messenger RNAs can travel from these sealed replication compartments to the cytosol to ensure their translation and the assembly of progeny virions. In this study, we used cellular cryo-electron microscopy to visualize a molecular pore complex that spans both membranes of the double-membrane vesicle and would allow export of RNA to the cytosol. A hexameric assembly of a large viral transmembrane protein was found to form the core of the crown-shaped complex. This coronavirus-specific structure likely plays a key role in coronavirus replication and thus constitutes a potential drug target.

4

A MOLECULAR PORE SPANS THE DOUBLE MEMBRANE OF THE CORONAVIRUS REPLICATION ORGANELLE

Introduction

Severe acute respiratory syndrome coronavirus 2 (SARS-CoV-2) is the third and most impactful example of a potentially lethal coronavirus infection in humans within the past 20 years (*7, 191, 192*). Coronaviruses are positive-stranded RNA (+RNA) viruses that replicate their unusually large genomes in the host cell's cytoplasm. This process is supported by an elaborate virus-induced network of transformed endoplasmic reticulum (ER) membranes known as the viral replication organelle (RO) (*52, 54, 55, 61*). Double-membrane vesicles (DMVs) are the RO's most abundant component and the central hubs for viral RNA synthesis (*61*). The DMV's interior accumulates double-stranded (ds) RNA, presumably intermediates of viral genome replication and subgenomic mRNAs synthesis (*55, 61*). DMVs may offer a favorable microenvironment for viral RNA synthesis and shield it from innate immune sensors that are activated by dsRNA. However, coronaviral DMVs have been characterized as compartments that lack openings to the cytosol (*54, 55, 61*), despite the fact that newly-made viral mRNAs need to be exported for translation. Moreover, the coronavirus genome needs to be packaged by the cytosolic nucleocapsid (N) protein, before being targeted to virus assembly sites on secretory pathway membranes (*42*).

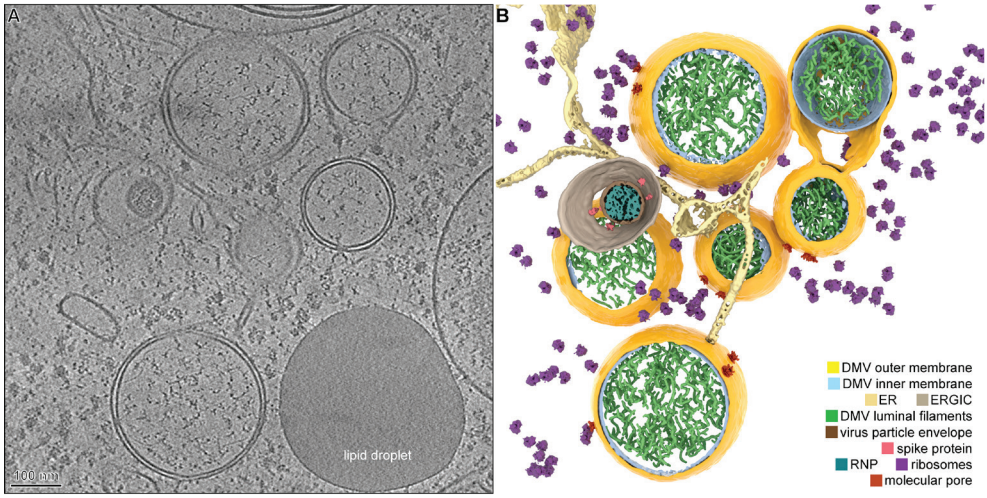

Figure 1. Coronavirus-induced DMVs revealed by cryo-ET. (A) Tomographic slice (7 nm thick) of a cryo-lamella milled through an MHV-infected cell at a middle stage of infection. (B) Three-dimensional (3D) model of the tomogram, with the segmented content annotated. See also movie S1. ERGIC, ER-to-Golgi intermediate compartment.

Results

In this study, we used cryo-electron microscopy (cryo-EM) to analyze the structure of coronavirus-induced ROs in their native host cellular environment. The murine hepatitis coronavirus (MHV) is a well-studied model for the genus *Betacoronavirus*, which also includes severe acute respiratory syndrome coronavirus (SARS-CoV), Middle East respiratory syndrome coronavirus (MERS-CoV), and SARS-CoV-2. One advantage of MHV over these class-3 agents is the absence of serious biosafety constraints, thus making MHV suitable for in situ cryo-EM studies. We performed electron tomography (ET) on cryo-lamellae prepared by focused ion beam milling of cells in the middle stage of MHV infection. The tomograms revealed abundant perinuclear DMVs with an average diameter of 257 ± 63 nm (±SD), occasionally interconnected or connected to the ER as part of the reticulovesicular network described

in previous work (Fig. 1, Fig. S1 and Movie S1) (*52, 54, 55, 61*). In addition, macromolecular features that had not been discerned in conventional EM samples became apparent (Fig. S2 to S4). The DMV lumen appeared to primarily contain filamentous structures that likely correspond to viral RNA (Fig. 1 and Fig. S4). In part, this is expected to be present as dsRNA (*55, 61*), as supported by the relatively long straight stretches observed in some of these filaments, consistent with the persistence length of dsRNA (*193*) (Fig. S4).

Each DMV contained multiple copies of a molecular complex that spanned both membranes, connecting the DMV interior with the cytosol (Fig. 2A, Supplementary Text). Such complexes were also found in DMVs in prefixed SARS-CoV-2-infected cells (Fig. 2B and Fig. S5). We surmise that this pore represents a generic coronaviral molecular complex that has pivotal role in the viral replication cycle. Most likely, it allows the export of newly synthesized viral RNA from the DMVs to the cytosol. Functionally analogous viral complexes used for RNA export include those in the capsids of the *Reoviridae* (*194*) and, notably, the molecular pore in the neck of the invaginated replication spherules induced by flock house virus (*172*). None of these complexes, however, are integrated in a double-membrane organelle.

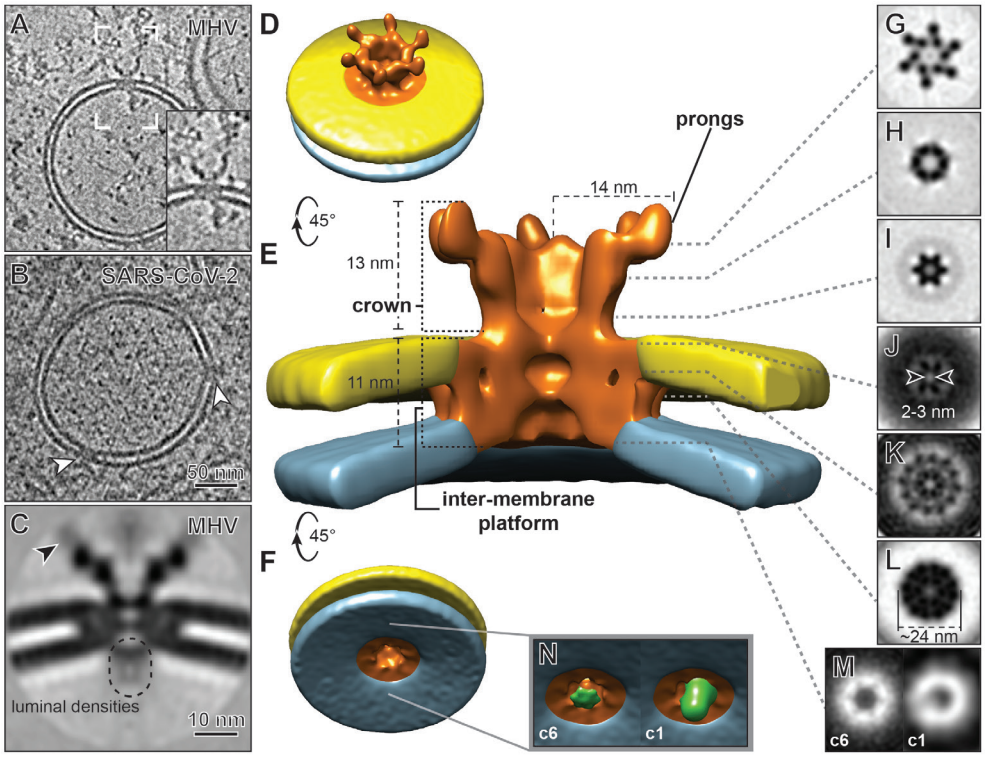

Figure 2. Architecture of the molecular pores embedded in DMV membranes. Tomographic slices (7 nm thick) revealed that pore complexes were present in both (A) MHV-induced DMVs and (B) prefixed SARS-CoV-2–induced DMVs (white arrowheads). The inset in (A) is a close-up view of the area delineated by white brackets. (C to L) Sixfold-symmetrized subtomogram average of the pore complexes in MHV-induced DMVs. (C) Central slice through the average, suggesting the presence of flexible or variable masses near the prongs (black arrowhead) and on the DMV luminal side. (D to F) Different views of the 3D surface-rendered model of the pore complex (copper colored) embedded in the outer (yellow) and inner (blue) DMV membranes. (G to L) 2D cross-section slices along the pore complex at different heights (see also movie S2). (M and N) An additional density at the bottom of the sixfold-symmetrized volume (c6, green) appeared as an off-center asymmetric density in the unsymmetrized average (c1).

Subtomogram averaging of the double-membrane-spanning complexes in MHV-induced DMVs revealed an overall sixfold symmetry (Fig. 2, Fig. S6 and Movie S2). A cytosolic crown-like structure extended ~13 nm into the cytosol and was based on a ~24-nm wide platform embedded in the DMV membranes. The two membranes did not fuse and maintained the typical DMV intermembrane spacing of ~4.5 nm (Fig. S2). The complex formed a channel that followed its sixfold axis. On the DMV luminal side, the channel started with a ~6-nm-wide opening, narrowed toward the cytosol, and had two tight transition points (Fig. 2, J and L). The one at the level of the DMV outer membrane (Fig. 2J) was the most constricted, with an opening of ~2 to 3 nm, but would still allow the transition of RNA strands. Toward the cytosolic space, the complex opened into a crown-like structure, exposing six cytosolic "prongs". With an achieved resolution of 3.1 nm, we roughly estimate that the complex has a total molecular mass of 3 MDa, of which the crown represents ~1.2 MDa (Fig. S6).

We then considered the possible constituents of this complex. Coronaviruses express two large replicase polyproteins that are proteolytically cleaved into 16 nonstructural proteins (nsps) (*195*). Three of these nsps — nsp3 (222 kDa in MHV), nsp4 (56 kDa), and nsp6 (33 kDa) — are transmembrane proteins and thus are potential candidates to be components of the pore. These nsps contain two, four and six transmembrane domains (TMDs), respectively (*196-198*) (Fig. 3A) and engage in diverse homotypic and heterotypic interactions (*199*) thought to drive the formation of double-membrane ROs (*44, 45, 116*). On the basis of its size, the multidomain MHV nsp3 subunit is an attractive putative constituent of the pore. MHV nsp3 consists of a large cytosolic region of ~160 kDa followed by two TMDs and a C-terminal cytosolic domain of ~41 kDa (*196*). Whereas the TMDs and C-terminal domain are highly conserved, the domain composition and size of the N-terminal part of nsp3 is quite variable among coronaviruses (*199, 200*). Several nsp3 domains including the conserved N-terminal

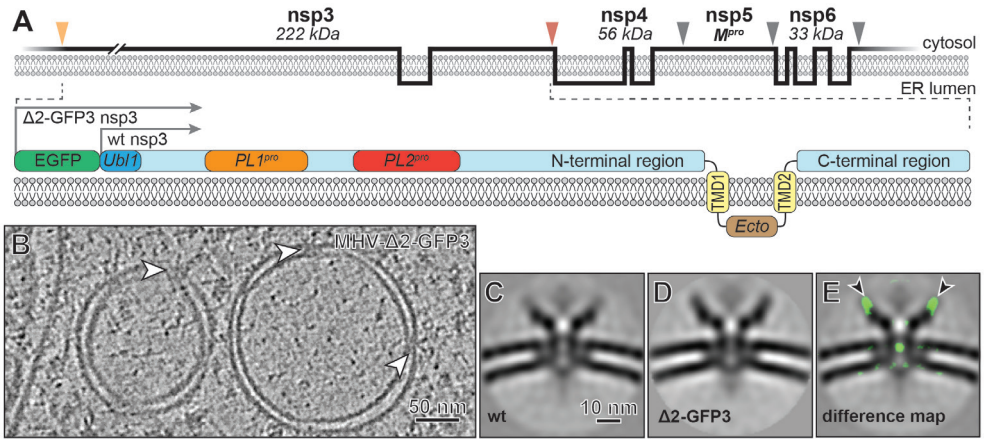

Figure 3. The coronavirus transmembrane protein nsp3 is a component of the pore complex. (A) (Top) Membrane topology of MHV transmembrane nsps, with protease cleavage sites indicated by orange (PL1pro), red (PL2pro), and gray (Mpro) arrowheads. (Bottom) Detailed depiction of nsp3, showing some of its subdomains and the position of the additional EGFP moiety present in MHV-Δ2-GFP3. PLpro, papain-like protease; Mpro, main protease. (B) Tomographic slice of DMVs induced by MHV-Δ2-GFP3, with embedded pore complexes (white arrowheads). (C and D) Comparison of the central slices of the sixfold-symmetrized subtomogram averages of the pore complexes in DMVs induced by (C) wild-type (wt) MHV and (D) MHV-Δ2-GFP3. (E) Density differences of 3 standard deviations between the mutant and wild-type structures, shown as a green overlay over the latter, revealed the presence of additional (EGFP) masses in the mutant complex (black arrowheads; see also movie S3).

ubiquitin-like domain 1 (Ubl1, 12.6-kDa) that binds both single-stranded (ss) RNA (*201*) and the N protein (*202, 203*), may interact with viral RNA (*199*).

To investigate whether nsp3 is a component of the DMV molecular pore, we imaged cells infected with a well-characterized engineered MHV expressing nsp3 with an enhanced green fluorescent protein (EGFP) moiety fused to the Ubl1 domain [MHV-Δ2-GFP3 (*204*)] (Fig. S7). This mutant lacks nsp2, which is dispensable for replication in cell culture (*205*). Subtomogram averaging of the pore complexes in these samples (Fig. 3B) revealed the presence of six additional densities on top of the prongs, each representing a mass compatible with that of EGFP (Fig. 3C-E, Movie S3). These results identified nsp3 as a major constituent of the complex and provided insights into its orientation, with the Ubl1 domain residing in the prongs. Six copies of nsp3 can be envisioned to constitute most of the cytosolic crown-like structure (~1.2 MDa). Other viral and/or host proteins and lipids are probably also part of the ~1.8 MDa intermembrane platform, with nsp4 and nsp6 being prominent candidates. Notably, different studies suggest that nsp3-nsp4 interactions drive membrane pairing and determine DMV biogenesis and morphology (*44, 45, 116, 206*).

The molecular pores frequently appeared to interact with other macromolecules on both the cytosolic and DMV luminal sides (Fig. S8). In the subtomogram averages, these appeared as largely blurred out densities (Fig. 2C), which suggests that the interactions are dynamic. (Fig. 2C). A small region on the luminal side however, had relatively higher density, and was resolved in the unsymmetrized average as a closely associated and slightly off-center mass (Fig. 2M and N, and Fig. S6D). We speculate that this mass may be part of the viral replication machinery. The coronaviral replication/transcription complex (RTC) is thought to consist of a subset of relatively small (~10 to 110 kDa) nsps with the RNA-dependent RNA polymerase (nsp12) at its core (*207-209*). However, some of these subunits may associate with the RTC only transiently and the nsp stoichiometries of the complex are unknown. The luminal partners of the pore complex, prominent as masses varying in shape and size, appeared to interact with the putative RNA content of the DMVs (Fig. S8).

The interaction partners of the cytosolic nsp3 prong ranged from chain-like masses to larger assemblies (Fig S8, black arrowheads). The subdomains of the long N-terminal nsp3 domain engage in a range of viral and virus-host interactions (*199, 200*); consequently, the list of possible interactors is substantial. Among them, the viral N protein (55 kDa), which binds to the nsp3 Ubl1 domain (*202, 203*), is a prominent candidate. The Ubl1-N interaction has been proposed to target viral RNA to replication sites at early stages of infection (*203*), but it may also modulate RNA exit and encapsidation on the cytosolic side of the pore complex. Notably, DMV-rich regions of the cytosol were crowded with protein assemblies that had a diameter of ~15 nm (Fig. S9). These proteins strongly resembled the nucleocapsid structure in coronavirus particles, a helical ribonucleoprotein (RNP) complex that consists of the RNA genome and N protein oligomers (*210*) (Fig. S9).

Discussion

Our findings suggest a pathway for newly made viral genomic RNA from the DMV interior, via the channel of the pore, to the cytosolic sites of encapsidation. In our model, specific replicase subunits may associate with the pore complex to guide the newly synthesized RNA toward it (Fig. 4A). As proposed for other +RNA viral ROs (*172*), only +RNAs would need to be exported, whereas negative-stranded templates and/or dsRNA intermediates could remain inside the DMVs. On the cytosolic side, all exported viral mRNAs may associate with

the N protein (Fig. 4B). Alternatively, the accumulating N protein could serve to select part of the newly made genomes for packaging. The remainder would then be used for translation, together with the much smaller, though much more abundant, subgenomic mRNAs (*211*). Genome-containing RNP complexes would travel to the membranes where the viral envelope proteins accumulate and engage in the assembly of progeny virions (Fig. 4C) (*212*). These bud into single-membrane compartments (Fig. 4D), typically derived from the ER-to-Golgi intermediate compartment (*42*), and travel along the secretory pathway to be released into extracellular space.

The double-membrane–spanning molecular pore revealed here may constitute the exit pathway for coronaviral RNA products from the DMV's interior toward the cytosol, with the large and multifunctional nsp3 being its central component. Although the exact mode of function of this molecular pore remains to be elucidated, it seems to be a key structure in the viral replication cycle that is likely conserved among coronaviruses and thus may offer a coronavirus-specific drug target.

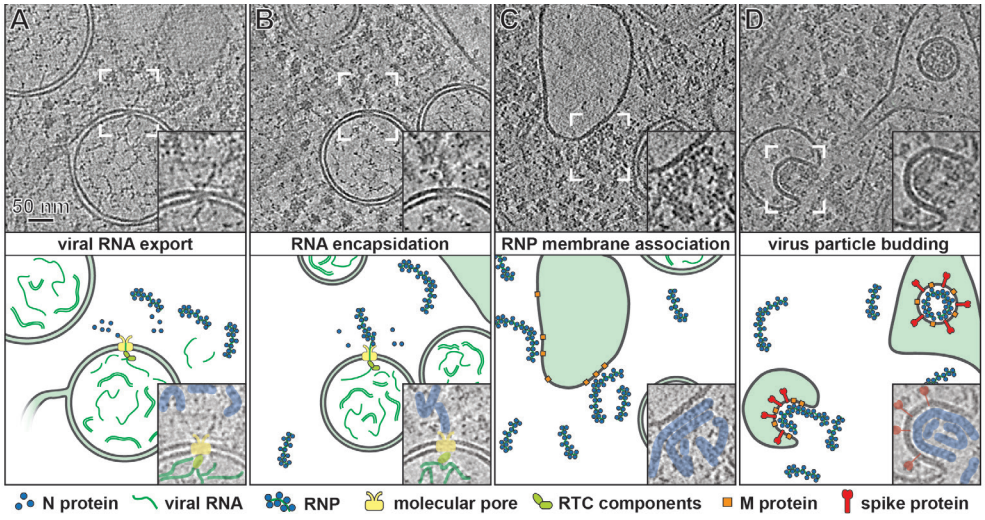

Figure 4. Model of the coronavirus genomic RNA transit from the DMV lumen to virus budding sites. Tomographic slices from MHV-infected cells (top) highlight the respective steps in the model (bottom). (A) The molecular pore exports viral RNA into the cytosol, (B) where it can be encapsidated by N protein. (C) Cytosolic RNP complexes can then travel to virus assembly sites for membrane association and (D) subsequent budding of virions. The insets in the top panels provide close-up views of the areas delineated by white brackets.

Materials and methods

Cell culture, infection and vitrification

17clone1 and Vero E6 cells were grown as described previously (*61*). R1/4 gold Quantifoil grids (200 mesh, Quantifoil Micro Tools, Jena, Germany) were cleaned overnight by placing them on a chloroform-soaked filter paper in a sealed glass dish. After drying, the grids were glow-discharged and placed in 3.5-cm diameter cell culture dishes (Greiner Bio-One, Frickenhausen, Germany) containing PBS. After UV-sterilization for 30 min in a laminar flow cabinet, PBS was removed and 110,000 17clone1 or Vero E6 cells were seeded per dish and incubated overnight at 37 °C. 17clone1 cells were infected with wild type (wt) MHV (ATTC VR-764) or MHV-Δ2-GFP3 (*204*). In the MHV-Δ2-GFP3 mutant (generously provided by Mark Denison, Vanderbilt University Medical Centre, Nashville, TN, USA), the nsp2-coding region, which is dispensable for virus replication in cell culture (*205*), is replaced by the EGFPcoding sequence, yielding a GFP-nsp3 fusion protein (*204*). Samples were plunge-frozen in liquid ethane at 8 h post-infection (p.i.) (wt MHV) or 10 h p.i. (MHV-Δ2-GFP3) with a Leica EM GP automated plunge-freezer (Leica microsystems, Wetzlar, Germany), after applying 15 s of blotting from the backside of the grid and 1s post-blotting time in conditions of 37 °C and 95% humidity. VeroE6 cells were infected with SARS-CoV-2 isolate BetaCoV/Australia/VIC01/2020 (GeneBank ID: MT007544.1; kindly provided by Leon Caly and Julian Druce, Doherty Institute, Melbourne, Australia (213)) and chemically fixed at 8 h p.i. with 3% PFA in cell culture medium. After 1 h, the original fixative was replaced by 0.5% PFA in cell culture medium and the samples were stored overnight at 4 °C, before being exported from the biosafety level 3 facility of Leiden University Medical Center, the Netherlands. Next, they were incubated in PFA-free medium for 30 min, plunge-frozen in liquid ethane using a Leica EM GP with 10 s blotting, 2 s post-blotting time and chamber conditions of 21 °C and 90% humidity, and stored in liquid nitrogen until further use.

Electron cryo-tomography

Plunge-frozen samples were transferred to an Aquilos cryo-focused ion beam scanning electron microscope (FIB-SEM) (Thermo Fisher Scientific, Hillsboro, OR, USA) and cryo-lamellae were prepared as described (*214*). For the MHV-Δ2-GFP3 samples, prior to FIB-milling cryo-fluorescence light microscopy (cryo-FLM) was performed on an upright FLM-system (Axioimager Zeiss, Oberkochen, Germany) equipped with a cryo-correlative light and EM stage (CMS196, Linkam, Tadworth, UK). The resulting images were integrated in the FIB-milling workflow using MAPS software (Thermo Fisher Scientific) to guide the finding of suitable milling regions (Fig. S8). A total of approximately 200 cryo-lamellae of 120-200 nm thickness were prepared (139 for wt MHV, 32 for MHV-Δ2-GFP3, 23 for SARS-CoV-2), of which about 40% contained the features of interest and were also of a sufficient quality to allow tomographic data collection. Tilt-series acquisition was carried out on FEI Titan Krios (Thermo Fisher Scientific) electron microscopes operated at 300 kV and equipped with a Gatan GIF Quantum energy filter (Gatan, Pleasanton, CA). Movie frames were collected using a Gatan K2 (MHV data) or Gatan K3 (SARS-CoV-2 data). The summit direct detection devices were operated in counting mode. Zero-loss imaging with a 20-eV slit width was done with a pixel size of 3.51 Å or 3.37 Å (MHV and SARS-CoV-2 data, respectively) and defocus values ranging from-5 to-8 µm. Bi-directional or dosesymmetric (*215*) tilt series were collected with FEI Tomo4 and serialEM software, respectively. The total dose applied on the sample was 120-140 $e^{-}/Å^{2}$, which was distributed over tilt series covering a 100˚-120˚ range with 2˚ or 3˚ tilt increments. Recorded movie frames were aligned with MotionCor2 using 5 x 5 patches

(*188*). The resulting fiducial-free tilt-series were aligned and SART (Simultaneous Algebraic Reconstruction Technique) reconstructed using 9 SART iterations with AreTomo (Zheng and Agard, https://msg.ucsf.edu/software). CTF-estimations were performed with CTFFIND4 (*216*), while CTF-correction and denoising for visualization and modeling purposes was done with the ctfphaseflip (*217*) and the nonlinear anisotropic diffusion (*218*) packages included in IMOD (*219*), respectively.

Subtomogram averaging

Individual DMV-embedded molecular pores were manually picked from 4-times binned tomograms using the IMODs 3dmod interface. The coordinates were then transferred into Dynamo (*220*), which was used for particle cropping, alignment and averaging from 2-times binned tomograms (7.02 Å per pixel). For the wt MHV sample, 611 particles (96 pixels box size) were extracted out of the 53 highest quality tomograms (from 33 lamellae), while for the MHV-Δ2-GFP3 sample 154 particles out of 31 tomograms were cropped (from 16 lamellae). The initial alignment allowed full rotational search in all directions and resulted in a rough average that was manually centered onto the central z-axis to establish the shift to be applied to the individual particles. This was followed by a center-refinement step using the 20-fold symmetrized average as a reference to fine align the particles on the central axis. Subsequent alignment steps allowed only azimuthal rotations and limited lateral shifts. For the wt MHV sample, three subsets of random particles were used to generate averages for multi-reference alignment, which resulted in a class of 346 particles that provided the highest resolution and were included in the final averages. The discarded particles likely represent different conformational states of the complex that, nevertheless, appeared to be insufficiently populated to provide further insight at this stage. Two parallel alignments were carried out with the selected particles, with or without applying sixfold symmetry. A tight missing wedge mask that removed all information beyond ± 40˚ in Fourier space was applied to all the particles during alignment. The Fourier shell correlation curves were determined from individually refined half-datasets of the wt MHV and MHV-Δ2-GFP3 subtomogram averages, respectively. Local resolution maps were generated using the ResMap software (*221*).The correct handedness of the averages was assessed by comparison with an average of aligned ribosome particles originating from our data to a published ribosome structure (*222*).

3d modeling and model interpretation

3D surface models of the DMVs in the cellular environment were created in Amira (Thermo Fisher Scientific) and animations in Cinema4D (Maxon Computer, Friedrichsdorf, Germany) software. Model files of ribosomes and pore complexes integrated in these renderings were obtained with Dynamo, in the case of the molecular pores, from the density map and coordinates generated during sub-tomogram averaging, and in the case of ribosomes by template matching with a ribosome average originating from our data.

Surface models of the pore complex were generated in UCSF Chimera software (*223*) from 3d averages low-pass filtered to the resolution achieved by sub-tomogram averaging. The contour level for the surface rendering of the complex was chosen so that the crown would best resemble the appearance of this region in the density map (Fig. 2C, G-I). Molecular weight estimations were done by calculating the (sub)volumes enclosed by the surface models generated in Chimera and dividing them by the average density of globular proteins (*224*). For the generation of difference maps of the averages from the molecular pores

found in cells infected with wt MHV and MHV-Δ2-GFP3, the radial power spectra of the reconstructed volumes were adjusted to each other before subtracting the volumes using the relion_image_handler function in Relion 3.1 (*225*).

Acknowledgments

We thank M. Denison for sharing MHV-Δ2-GFP3, L. Caly and J. Druce for providing SARS-CoV-2 isolate betaCoV/Australia/VIC01/2020, N. Ogando for BSL3 assistance, F. Faas for technical support, S. Howes and T. Sharp for advice on image processing and helpful discussions, J. Plitzko and M. Schaffer for introducing us to cryo–focused ion beam milling, and J. Wolff, Y. van der Meer, and H. Friedrich for support during the lockdown. EM tomography data of MHV-infected samples were collected at the Netherlands Centre for Electron Nanoscopy (NeCEN) with assistance from C. Diebolder and R. Dillard.

Funding: Access to NeCEN was made possible through financial support from the Dutch Roadmap Grant NEMI (NWO grant 184.034.014). D.A.A. was supported by NIH grants R35GM118099 and U19 AI135990. S.Z. was supported by the Howard Hughes Medical Institute. K.G. was supported by BMBF grant 05K18BHA and DFG grants EXC 2155, INST 152/772-1, and INST 777-1 FUGG. E.J.S. was supported by the #wakeuptocorona crowdfunding initiative of the Leiden University Fund (LUF) and LUMC Bontius Foundation and by the SCORE project (European Union's Horizon 2020 research and innovation program, grant 101003627).

Data and materials availability: SARS-CoV-2 isolate betaCoV/Australia/VIC01/2020 and MHV-Δ2-GFP can be shared on request upon authorization from their original source (SARS-CoV-2: Leon Caly and Julian Druce, Doherty Institute, Melbourne, Australia; MHV-Δ2-GFP3: Mark Denison, Vanderbilt University Medical Centre, Nashville, TN, USA). Cryo-EM maps have been deposited in the Electron Microscopy Data Bank under accession codes EMD-11514 (wild-type MHV–induced molecular pore) and EMD-11515 (MHV-Δ2-GFP3–induced molecular pore).

Supplementary text

Number of molecular pores per DMV

To estimate the average number of molecular pores per DMV, 8 tomograms from 6 lamellae were used to count the number of pore complexes present in a total of 30 DMVs. Pores could be found in all the DMVs in the tomograms. The average number of detected pores (4.8 per DMV) was then extrapolated to account for the fact that only part of an average-sized DMV (257 nm in diameter, Fig. S1) is embedded in the thin cryolamella used for this quantification (~150 nm thick on average). This resulted in an estimate of ~8 pores per DMV, which can be considered a lower limit to the real number, as it does not take into consideration the missing-wedge effect intrinsic to electron tomography data that hampers the detection of molecular pores in certain orientations of the reconstructed volumes (*226*).

Supplementary figures

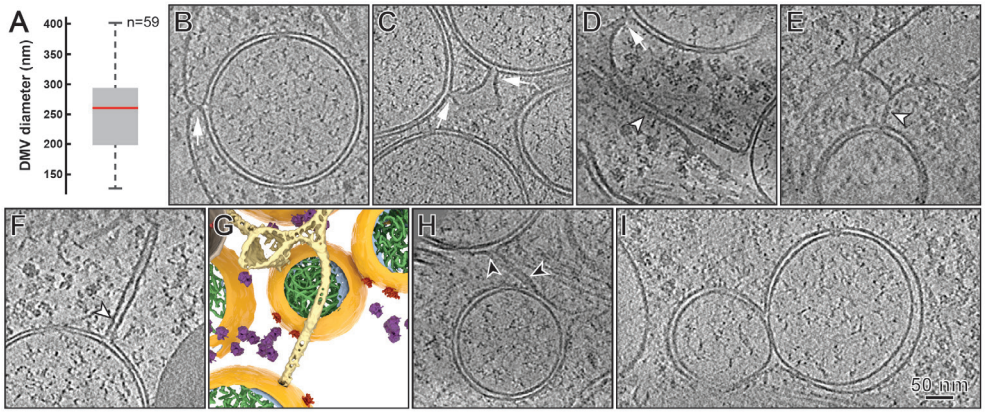

Figure S1. Overall morphology of the MHV-induced DMVs in cryo-lamellae. (A) Whisker plot of the size distribution of the DMVs as measured from the tomograms at the DMV equators. Most of the DMVs in the cryo-EM samples were clearly spherical, a subset of which was used for the plot. (B-G) Connections between the outer membrane of the DMVs and the ER were occasionally detected in the tomograms. These include the neck-like connections previously documented in resin-embedded specimens (*54, 55, 61*) (B-D, white arrows), and, strikingly, thus far unreported tubular connections reaching up to ~300 nm (D-F, white arrowheads). Some DMVs were clearly interconnected through the ER (C, D) or by a tubular connection (H, black arrowheads). While these different connections were only detected in a subset of DMVs, it should be noted that only a percentage (≤60%) of an average-sized DMV would be contained in the thin cryo-lamellae used in this study (~150 nm thick). These observations were consistent with the previous notion of coronavirus-induced DMVs being largely interconnected as part of a reticulovesicular network (*54, 55, 61*). (I) In some cases, DMVs appeared to fuse together through their outer membrane forming a so-called vesicle packet (*55, 211*). (B-F, H, I) 7-nm thick tomographic slices. (G) 3D rendering of the tubular connection in (F).

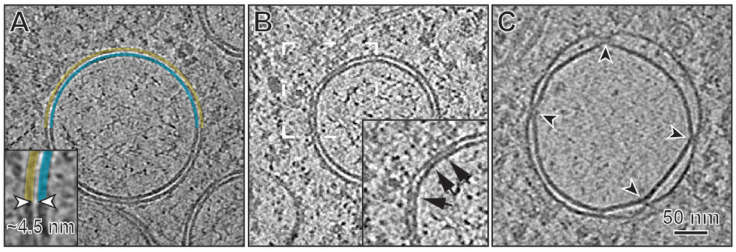

Figure S2. Membrane-membrane interactions in coronaviral DMVs. (A) The outer and inner membranes of MHV-induced DMVs were most commonly separated by a regular spacing of ~4.5 nm. Such regular spacing is likely to be mediated by the interactions of factors embedded in the inner and outer membrane. (B) In fact, densities crossing the luminal space between the two membranes (boxed area, black arrows) were frequently found in these regions. Notably, the transmembrane proteins nsp3 and nsp4 have been previously implicated in membrane pairing (*44, 45, 116*). Local deviations from the described regular inter-membrane spacing were common and, (C), occasionally, DMVs with largely dissociated membranes and molecular pores at constriction points (black arrowheads) were observed.

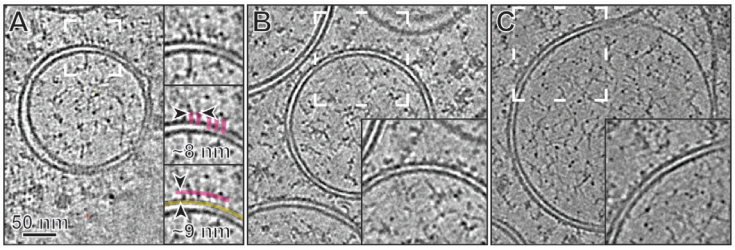

Figure S3. Macromolecular features on the outer DMV membrane. (A-C) The outer DMV membrane appeared frequently decorated with a variety of molecular features. A striking recurrent motif observed in the tomographic slices of the reconstructed DMVs were regular arrays (~8 nm spacing) of small globular masses at ~9 nm distance from the outer membrane to which they seemed to connect through a narrow link (boxed areas and insets). While the identity of these different densities could not be ascertained, it is worth noting that numerous viral and host proteins associate with coronavirus replication organelles (*170*) and that the nsp3 transmembrane protein contains multiple cytosolic domains that have been implicated in interactions with host factors (*200, 227*).

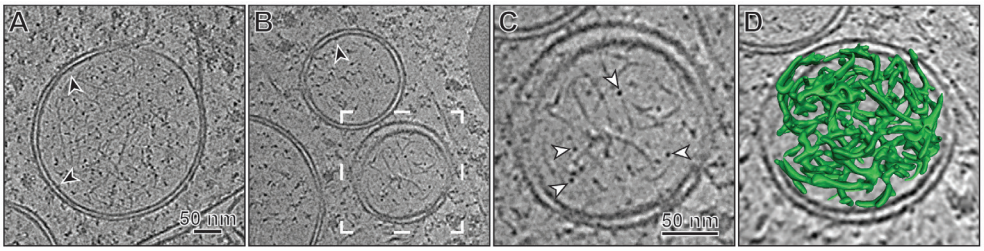

Figure S4. DMV content. (A-C) DMVs appeared to contain primarily filamentous structures, which could appear as dense points in the tomographic slices when viewed in cross-section (C, white arrowheads). The tomograms revealed relatively straight segments of a length consistent with the persistence length of dsRNA (*193*), which has been previously detected inside coronavirus-induced DMVs by immuno-EM (*55, 61*). The dsRNA filaments seemed to be loosely packed inside the DMVs forming what, at the current resolution, appeared as an inextricable mesh of filaments. While ssRNA or protein complexes like the RTC could be contained in the DMV lumen, their presence within this intricate filamentous mesh could not be ascertained. The inner DMV membranes were relatively devoid of distinct associated partners, with only occasional small interacting densities (black arrowheads). (A-C) 7-nm thick tomographic slices. (D) 3D model of the filamentous content inside the DMV shown in (C).

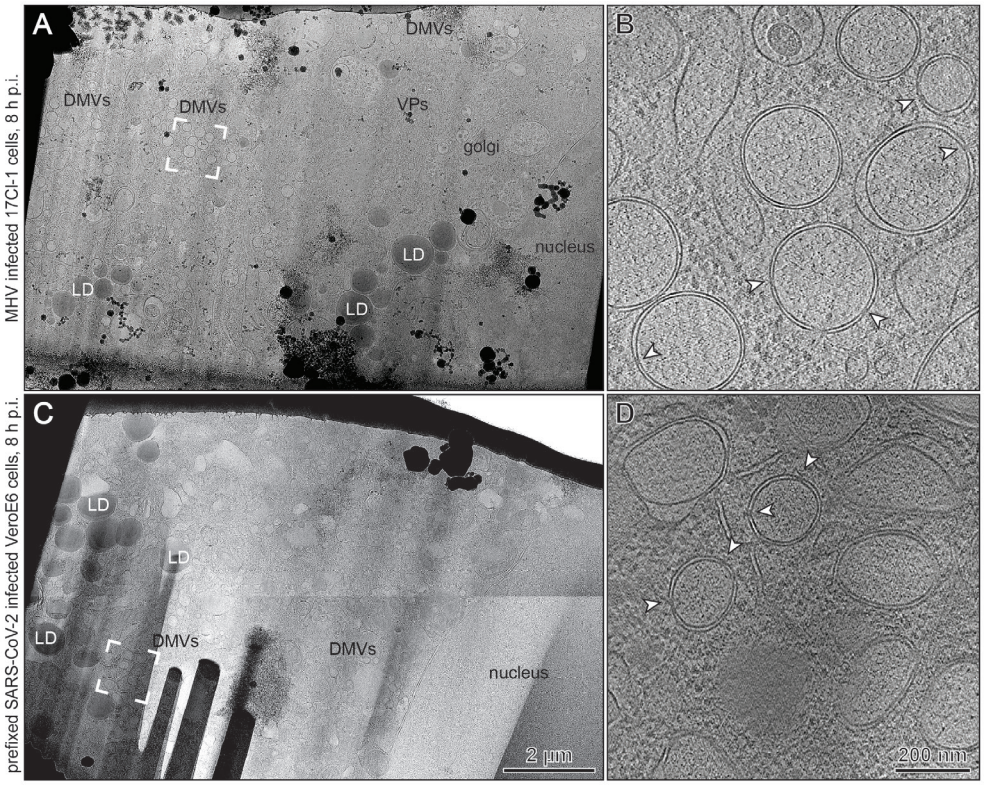

Figure S5. Electron tomography on cryo-lamella from coronavirus-infected cells. Cryo-lamellae generated from cells infected with wt MHV (A, B) and cells infected with SARS-CoV-2 (C, D) that were chemically fixed prior to vitrification. (A, C) Overviews of the cryolamellae, in which different structures, such as nucleus, mitochondria (M), the Golgi apparatus (Golgi), lipid droplets (LD), DMVs and virus particles (VPs), could be identified. (B, D) Slices (7 nm thick) of the tomograms reconstructed from tilt-series collected in the indicated regions (white frames in (A) and (C), respectively). Chemical fixation resulted in reduced contrast and produced morphological alterations in diverse organelles. Therefore, the partially distorted morphology of SARS-CoV-2-induced DMVs was likely also a result of fixation. Nonetheless, molecular pores in the DMV membranes could be identified for both samples (white arrowheads).

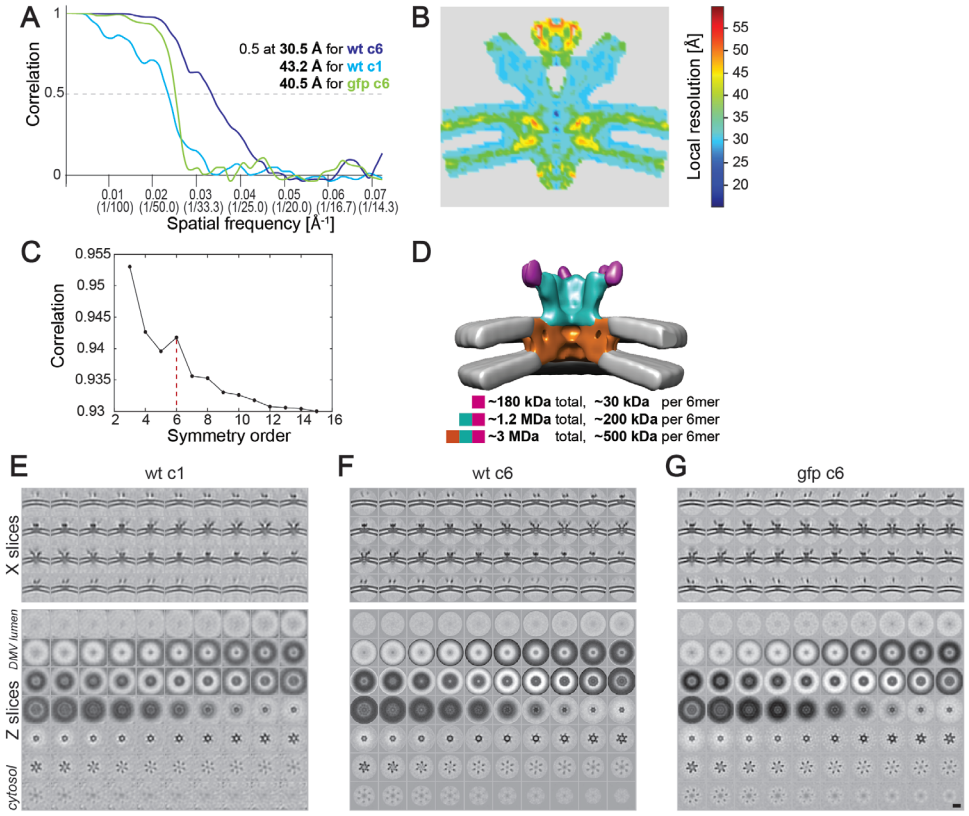

Figure S6. Subtomogram averaging of the DMV molecular pore. (A) Fourier shell correlation curves from molecular pore particles aligned without imposing symmetry (c1) or upon implying sixfold symmetry (c6). (B) Local resolution map showing lower resolution in the intermembrane platform relative to the crown of the complex. This suggested that this region has higher structural variability. (C) Plot of the correlation coefficients between unsymmetrized and symmetrized averages, highlighting the sixfold symmetry of the complex. (D) Estimates of the molecular masses of different sub-regions in the complex. (E-G) Slices (0.7 nm thick) throughout the molecular pore averages filtered to the achieved resolution, either parallel (top) or perpendicular (bottom) to the central axis of the complex. Wt, complex in wt MHV-induced DMVs; gfp, complex in MHV-Δ2-GFP3-induced DMVs. Scale bar (E-G) 10 nm.

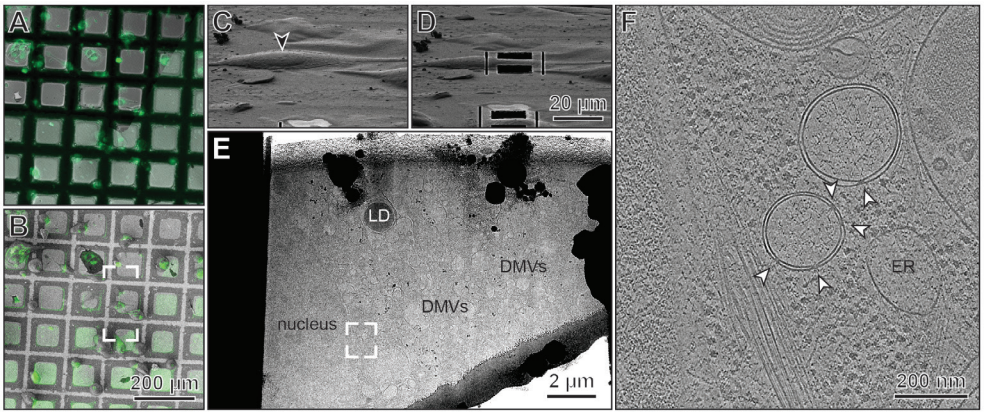

Figure S7. Cryo-EM imaging of MHV-Δ2-GFP3-infected cells was facilitated by cryo-correlative light microscopy. (A) Fluorescence nsp3-EGFP signal was observed in perinuclear regions of plunge-frozen infected cells, which served as a marker for regions containing virus-induced replication compartments (*52, 55*). (B) Overlays of the fluorescence signal on the corresponding SEM images guided the selection of suitable milling sites in the cryo-FIB-SEM machine. (C, D) The framed area in (B) as viewed from the FIB-beam direction before (C) and after (D) rough milling of the selected region. (E) Transmission EM overview of the thinned lamella, where regions of interest containing DMVs could be identified. The framed area was used for tilt-series acquisition. (F) A tomographic slice (7 nm thick) from the corresponding tomogram shows DMVs containing molecular pores (white arrowheads). LD, lipid droplet; ER, endoplasmic reticulum.

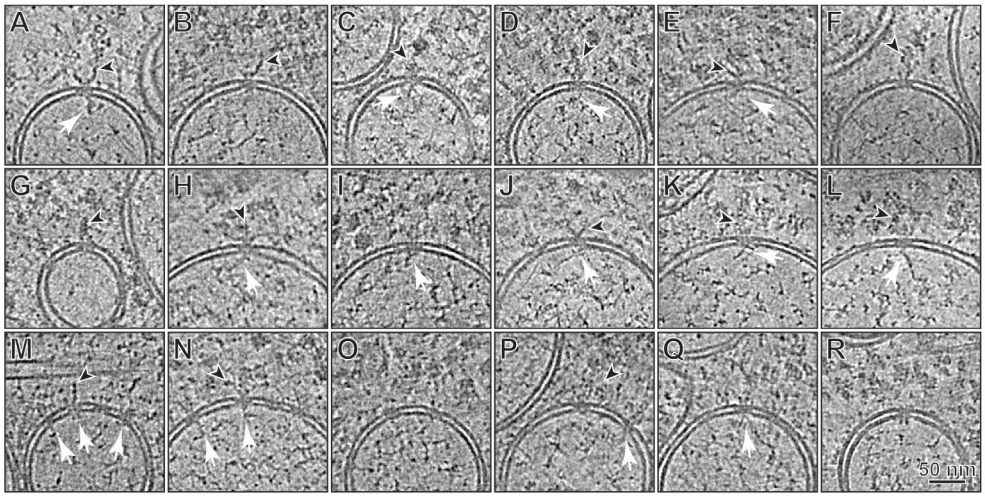

Figure S8. Gallery of molecular pores from 7 nm thick tomographic slices. (A-Q) Various macromolecular structures appeared to interact with both the cytosolic (top) and the DMV luminal (bottom) interfaces of the molecular pores. Cytosolic interaction partners (black arrowheads) range from (A, B, E) chain-like densities that seem to associate to the complexes prongs to larger assemblies that in some cases (D, G) are reminiscent of helical coronavirus RNPs. DMV luminal interaction partners (white arrows) appeared to vary in mass and shape as well, while they frequently also showed association to the DMV luminal filaments (C, D, I-L) assumed to be viral RNA. (R) In very few instances (less than 5 occurrences in a dataset containing more than 600 molecular pores) pore complexes that appeared to be inverted in the DMV membrane were observed.

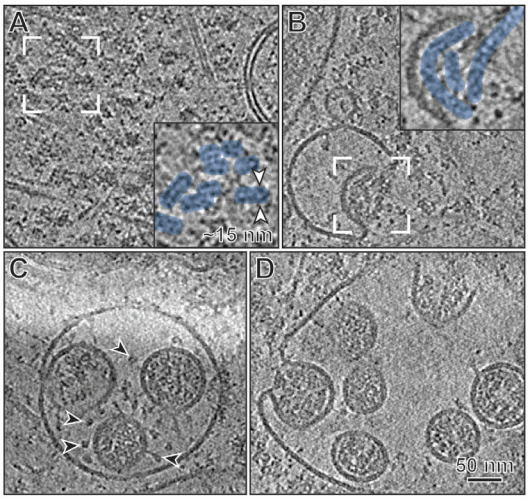

Figure S9. RNP assemblies in the cytosol and virions. Tomographic slices of 7 nm thickness showing (A) the abundant presence of cytosolic RNP assemblies in DMV-rich regions of the cytosol. The appearance of these structures is consistent with the helical coronavirus RNPs of ~15 nm in diameter previously described by single-particle analysis (210), and with the RNP observed inside coronavirus particles in tomographic data (C, D) (*173*). (B) RNP assemblies could associate to smooth-membrane compartments (boxed area) where they appeared to initiate the budding of virions into the lumen (*42*). (C-D) Budding virus particles containing RNP. Note also the spike protein on newly formed virions (C, black arrowheads).

Supplementary movies

Supplementary movies are available at:

https://science.sciencemag.org/cgi/content/full/science.abd3629/DC1

Movie S1.

Cryo-ET of MHV-induced ROs. Tomographic reconstructions and 3D segmented model of the region in a MHV-infected cells shown in Fig. 1.

Movie S2.

Subtomogram average of the molecular pore present in the DMVs induced by wt MHV. Sections through the sixfold symmetrized volume filtered to the final resolution. The slices (0.7 nm thick) are shown from the cytosolic side and are perpendicular to the central axis of the complex.

Movie S3.

Comparison of the wt and mutant Δ2-GFP3 molecular pore. The movie alternates between the central transversal slices through both subtomogram averages, filtered to the resolution of the Δ2-GFP3 reconstruction. Besides the additional densities on the top of the prongs in the mutant complex, conformational variations in the inter-membrane platform become apparent.

A MOLECULAR PORE SPANS THE DOUBLE MEMBRANE OF THE CORONAVIRUS REPLICATION ORGANELLE